buildings

MDPI

Article

Steel-Wire Mesh Reinforcement of Topology-Optimized 3D-Printed ECC Beams: Experimental and Numerical Investigation

Manfang Lin [1], Fan Yu [1], Zheng Yang [2], Yunqi Jiang [1], Lingzhi Li [1], Fei Teng [1,3], Ahmadi Mahfouz [4] and Xiang Li [2,*]

[1] College of Civil Engineering, Tongji University, Shanghai 200092, China
[2] State Grid Electric Power Engineering Research Institute Co., Ltd., Beijing 100055, China
[3] Shanghai Investigation, Design & Research Institute Co., Ltd., Shanghai 200434, China
[4] Faculty of Hydrotechnical Construction, "Tashkent Institute of Irrigation and Agricultural Mechanization Engineers" National Research University, Tashkent 100000, Uzbekistan
* Correspondence: axiang_bj@163.com

Abstract

Engineered cementitious composites (ECC) exhibit tensile strain hardening and multiple cracking, providing an inherent self-reinforcing capability that endows ECC with suitability for the complex forms enabled by topology optimization and 3D printing. To extend such optimized structures to a broader range of engineering applications, their structural capacity needs to be further enhanced through reinforcement. This study investigates two printable topology-optimized (TO) 3D-printed ECC beams in unreinforced and steel-wire-mesh-reinforced forms under four-point bending. For the single specimen tested in each configuration, steel-wire mesh increased the experimental peak loads of TO1 and TO2 by 53.7% and 81.2%, respectively. After normalization by the measured as-built retained-area ratio, the corresponding increases in normalized peak load were 46.3% and 56.2%. Reinforcement produced contrasting effects on energy absorption, decreasing it by 36.8% for TO1 but increasing it by 47.2% for TO2. A three-dimensional finite-element model was developed to reproduce the printable geometries, extrusion discontinuities, and inter-filament and interlayer interfaces. The simulations showed that increasing reinforcement shifted the failure mode from distributed lower-chord cracking to damage at diagonal-to-chord connections and support-side interfaces. Increasing the normal interface strength from 1.0 to 2.5 MPa markedly improved the load capacity of both beam configurations, while a further increase to 4.0 MPa had a slight influence. These findings extend topology-optimized 3DP-ECC beyond geometry-driven material reduction toward reinforcement-enabled structural performance enhancement, providing a basis for the broader application of lightweight, high-capacity, and material-efficient 3D-printed structural systems.

Keywords: engineered cementitious composites; 3D concrete printing; topology optimization; numerical simulation; steel-wire mesh

Check for updates

Academic Editor: Salvatore Verre

Received: 3 October 2026
Revised: 21 October 2026
Accepted: 23 October 2026
Published: 26 October 2026

Copyright: © 2026 by the authors. Licensee MDPI, Basel, Switzerland. This article is an open access article distributed under the terms and conditions of the Creative Commons Attribution (CC BY) license.

1. Introduction

Extrusion-based 3D concrete printing (3DCP) has developed rapidly as a digital construction technology capable of fabricating cementitious components directly from computer-generated geometries. By eliminating conventional formwork and enabling automated material placement, 3DCP can reduce labor demand, construction waste, and the geometric restrictions associated with traditional casting. More importantly, extrusion-based fabrication makes non-prismatic, hollow, branching, and spatially varying structural forms practically achievable [1–4]. This geometric freedom provides an opportunity not

only to automate conventional construction but also to reconsider how structural material is distributed within load-bearing members.

Topology optimization is well suited to 3DCP because material can be retained only where it contributes to structural load transfer. Unlike conventional sectional optimization, topology optimization determines the spatial distribution of material within a prescribed design domain according to structural objectives and constraints, thereby removing mechanically inefficient regions while retaining the principal load-transfer paths [5–7]. Its application to concrete structures has historically been restricted by the difficulty and cost of fabricating complex optimized geometries using conventional molds. Additive manufacturing reduces this fabrication constraint and makes it possible to translate optimized geometries into physical components [8,9]. For cementitious structures, such material redistribution is especially attractive because reductions in structurally redundant concrete can simultaneously decrease self-weight and material consumption.

Recent studies have increasingly combined topology optimization with 3D concrete printing. Bi et al. [10] incorporated manufacturing requirements including self-support, continuous extrusion, anisotropy, and modular fabrication into a topology-optimization framework. Yang et al. [11] further considered nozzle-scale and path-continuity constraints to improve the compatibility between optimized geometries and extrusion-based fabrication. Hernández Vargas et al. [12] demonstrated internal topology optimization of printed concrete beams while maintaining their external geometry, and Silva et al. [13] experimentally fabricated topology-optimized deep beams with substantial material reduction. Other recent studies have combined optimized structural forms with lattice systems and manufacturing constraints [14,15]. These studies show that topology optimization can use the geometric freedom of 3DCP to produce load-bearing forms that would be difficult to fabricate using conventional molds.

The performance of these optimized geometries also depends on the tensile behavior of the printable material. Conventional printable cementitious materials have relatively limited tensile deformability, whereas the incorporation of traditional reinforcing bars during continuous extrusion can interrupt the printing process, restrict nozzle movement, and reduce geometric freedom [16–18]. Engineered cementitious composites (ECC) provide a suitable alternative. Through fiber bridging, tensile strain hardening, and distributed multiple cracking, ECC can sustain substantially larger tensile deformation than ordinary cementitious materials [19–22]. Printable ECC formulations have successfully combined these characteristics with the extrudability and buildability required for additive manufacturing, and structural-scale investigations have demonstrated their suitability for flexural members [23–25].

These characteristics make 3DP-ECC suitable for topology-optimized members containing narrow chords and discrete load paths. Topology optimization concentrates material in mechanically effective regions, while the tensile ductility of ECC enables highly reduced sections and discrete structural members to tolerate cracking without relying entirely on conventional steel reinforcement. Compared with ordinary printable concrete, the higher tensile deformability of ECC allows optimized members to sustain cracking with less reliance on conventional reinforcement. Nevertheless, extrusion introduces filament boundaries and layerwise interfaces whose properties are affected by filament geometry, fiber orientation, deposition sequence, and interlayer bonding [26–28]. These process-dependent features become increasingly important as material redundancy is reduced.

When higher flexural resistance is required, additional reinforcement is still needed [29]. Reinforcement strategies investigated for 3DCP include conventional bars, cables, post-tensioning, steel-wire meshes, textile reinforcement, and fiber-reinforced polymer meshes. Gebhard et al. [30] investigated several longitudinal and interlayer reinforcement strategies

for printed concrete beams, while Liu et al. [31] demonstrated the effectiveness of steel-wire mesh in improving flexural response. Steel-wire mesh has also been used in 3DP-ECC beams and was found to improve their flexural response [32,33].

Reinforcement has recently begun to be integrated with topology-optimized printed structures. Wang et al. combined topology optimization, reinforcement design, and structural evaluation for 3D-printed concrete truss beams [34], while subsequent work introduced three-dimensional reinforcement schemes for improved transverse force transfer [35]. These studies establish the feasibility of reinforced topology-optimized printed members. However, experimental evidence remains limited for highly material-reduced 3DP-ECC members reinforced at very low steel ratios, particularly when the same reinforcement strategy is applied to different printable realizations of an optimized topology. The extent to which printed interfaces constrain the structural benefit provided by reinforcement also remains insufficiently quantified.

To address this gap, this study investigates steel-wire-mesh reinforcement of two printable 3DP-ECC beam configurations reconstructed from the same low-material topology. The two geometries are tested in both unreinforced and reinforced forms, together with a full-section printed reference beam. Four-point-bending tests and digital image correlation are used to evaluate crack development, resistance, deformation, and energy absorption, while the measured as-built material content is introduced to assess structural efficiency. A three-dimensional finite-element model reproducing the actual toolpath geometry, extrusion discontinuities, and individual printed interfaces is subsequently validated against the experiments. Parametric analyses of reinforcement ratio and interface strength are then conducted to determine how changes in tensile reinforcement alter the governing force-transfer and failure mechanisms.

2. Experimental Program

2.1. Materials

The ECC mixture consisted of ordinary Portland cement (OPC), Class F fly ash (FA), silica fume (SF), silica sand, crumb rubber (CR), water, a polycarboxylate-based high-range water reducer (HRWR), and polyethylene (PE) fibers. The mass proportions of OPC, FA, SF, sand, CR, and water, normalized by the total binder mass, were 0.476, 0.439, 0.086, 0.179, 0.041, and 0.264, respectively. The HRWR dosage was 0.25% of the binder mass, and the PE fiber volume fraction was 1.5%. The printability of this ECC mixture and its suitability for fabricating 3D-printed structural beams have been demonstrated in previous studies [32,36]. Figure 1 shows the direct tensile stress–strain responses of three dog-bone specimens printed and tested along the filament direction. Their average tensile strength and tensile strain capacity were 4.82 MPa and 4.25%, respectively. The average compressive strength of three companion cast ECC cubes was 44.6 MPa, and the elastic modulus was 20 GPa.

High-strength steel-wire mesh was used as tensile reinforcement. Its principal mechanical properties are summarized in Table 1 [32], and the mesh configuration is shown in Figure 2. Each longitudinal wire bundle had a cross-sectional area of 0.5 mm^2. The mesh was designed as a unidirectional tensile reinforcement system, with the steel-wire bundles providing the load-carrying capacity in the longitudinal direction. The transverse polymer yarns served only to maintain the spacing and relative position of the steel-wire bundles and were not considered to contribute to the structural tensile resistance.

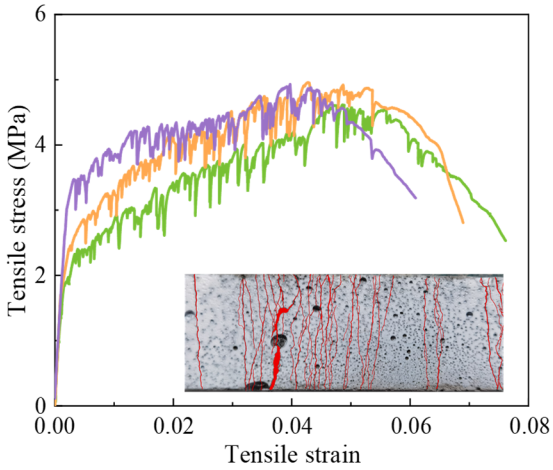


Figure 1. Tensile stress–strain response of 3DP-ECC.

Table 1. Specifications of steel-wire mesh.

Elastic Modulus (GPa)	Tensile Strength (MPa)	Ultimate Strain (%)	Density (g/cm^3)	Cross-Sectional Area per Bundle (mm^2)
150	3000	2.00	7.85	0.5

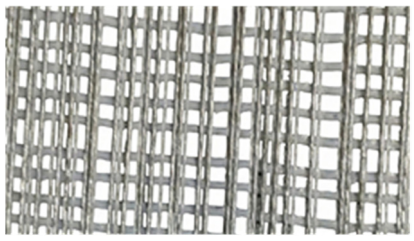


Figure 2. Configuration of the steel-wire mesh.

2.2. Topology Optimization and Specimen Design

The parent layout was obtained in ABAQUS by minimizing strain energy under an upper retained-volume constraint of 30%. The simply supported design domain reproduced the 800 mm span and 200 mm loading-point spacing of the four-point-bending tests. The optimization employed 10 mm elements and a sensitivity-based SIMP approach with a penalization factor of 3. The automatic filtering at a nominal default radius was about 1.3 times the element size. No explicit minimum-member-size constraint was prescribed. The 30% fraction was selected as the lowest practically printable retention level identified in preliminary reconstruction trials with an approximately 20 mm minimum effective filament width. It is not claimed to be a universally optimal fraction. Because the numerical density field could not be fabricated directly by extrusion, it was reconstructed into two finite-width printable configurations, denoted TO1 and TO2, as shown in Figure 3. Both configurations originated from the same parent topology but differed in local member arrangement and effective filament width. Their unreinforced forms served as baseline specimens, while the corresponding steel-wire-mesh-reinforced beams were denoted TO1-R and TO2-R. A full-section printed beam, Ref, was included as the reference specimen. The paired TO1/TO1-R and TO2/TO2-R specimens were designed to assess the effect of reinforcement within each printable configuration. The unreinforced full-section beam provided a benchmark for absolute capacity; no reinforced full-section beam (Ref-R) or non-optimized equal-material control was included, and the study does not claim optimality over alternative layouts.

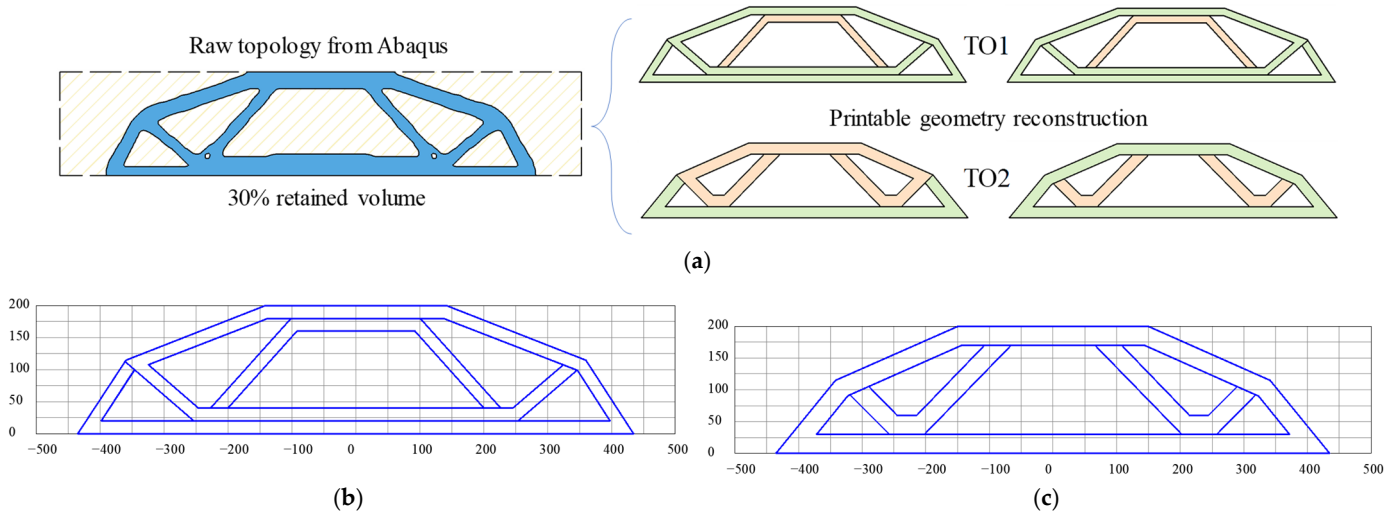


Figure 3. Reconstruction of the 30% parent topology into printable TO1 and TO2 geometries: (**a**) reconstruction of TO1 and TO2 from the original topology; (**b**) geometric dimensions of TO1; and (**c**) geometric dimensions of TO2 (unit: mm).

All beams had a nominal length of 1000 mm, width of 100 mm, and depth of 200 mm. The geometric and printing parameters of the specimens are summarized in Table 2. TO1 and TO1-R used an effective filament width of approximately 20 mm and a transverse layer increment of 15 mm, resulting in seven deposited layers through the beam width. TO2 and TO2-R used a 10 mm increment; the greater filament squeezing produced an effective filament width of approximately 30 mm and ten deposited layers. The two printable reconstructions thus differ simultaneously in member arrangement, effective filament width, layer increment, layer count, and interface distribution; their responses are compared at the configuration level rather than attributed to a single geometric variable.

Table 2. Specimen design and printing parameters.

Specimen	Effective Filament Width	Layer Increment	Layers	Layerwise Path Strategy	Nominal Reinforcement Ratio
Ref	20 mm	15 mm	7	Continuous serpentine path	-
TO1	20 mm	15 mm	7	Two alternating paths	-
TO2	30 mm	10 mm	10	Two alternating paths	-
TO1-R	20 mm	15 mm	7	Two alternating paths	0.10%
TO2-R	30 mm	10 mm	10	Two alternating paths	0.10%

Both TO1-R and TO2-R were reinforced with 40 longitudinal steel-wire bundles in total, which were cut from a mesh assembly into six pieces and placed symmetrically at six transverse interlayer planes within the lower tensile chord. Positioned within the bottom 20 mm of the beam with a spacing of approximately 2.5 mm, these bundles provided a total steel area of 20 mm^2 with an individual bundle area of 0.5 mm^2, resulting in a reinforcement centroid roughly 10 mm above the beam bottom. Because the material cross-section of the optimized beams varies along the span, a conventional local reinforcement ratio cannot be defined uniquely. A nominal reinforcement ratio was therefore calculated with respect to the complete 100 mm × 200 mm beam envelope, $\rho_s = A_s/(b_0 h_0)$, giving $\rho_s = 0.10\%$. The same definition is used in the numerical parameter study. The quoted 10 mm distance denotes the nominal reinforcement-centroid position, not a measured uniform clear-cover thickness; the local cover may vary with the deposited filament geometry.

2.3. Fabrication

All specimens were produced using the same extrusion system and a circular nozzle with a nominal outlet diameter of 20 mm. The full-section Ref beam was fabricated using a continuous serpentine trajectory in which adjacent longitudinal passes were connected by alternating turns at the beam ends, allowing the entire specimen to be deposited without intermediate extrusion interruption. For the optimized beams, extrusion followed the reconstructed structural members directly, and the two predefined toolpaths were alternated between adjacent layers. The printing speed was 30 mm/s, resulting in nominal printing durations of approximately 116.6 s and 93 s per layer for TO1 and TO2, respectively. All specimens were prepared using the same ECC batch, subjected to the same curing procedure, and tested at approximately one month of age.

For TO1-R and TO2-R, the steel-wire mesh was integrated during printing rather than attached after hardening. The mesh was positioned within the lower 20 mm region as successive layers were deposited, as illustrated in Figure 4.



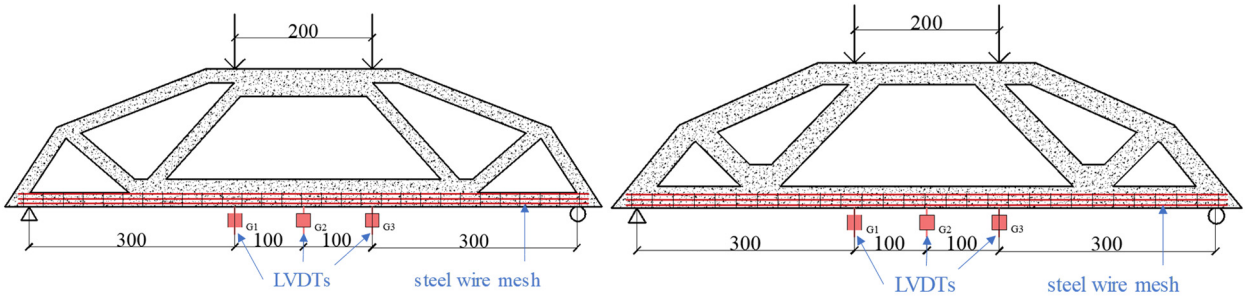
Figure 4. Fabrication process.

Owing to filament spreading, overlap at intersecting trajectories, and local deposition irregularities, the material quantity of the fabricated specimens differed from that of the reconstructed digital geometry. The designed retained-area ratio is denoted $R_d = A_d/A_0$, and the measured as-built ratio is denoted $R_a = A_a/A_0$, where A_d and A_a are the designed and measured solid areas in the longitudinal-depth plane, and A_0 is the corresponding area of the full-section reference geometry. These quantities are distinguished because R_d describes the printable design, whereas R_a represents the material actually present in the tested beam. The as-built area Aa was obtained by photographing the longitudinal–depth face, tracing the solid boundary in CAD, and calculating the enclosed solid area; A0 = 1000 × 200 mm^2. Because related deposition paths were repeated through the beam width, Ra provides an approximate relative ECC-volume indicator, consistent in trend with the available specimen weighing records.

2.4. Four-Point-Bending Test

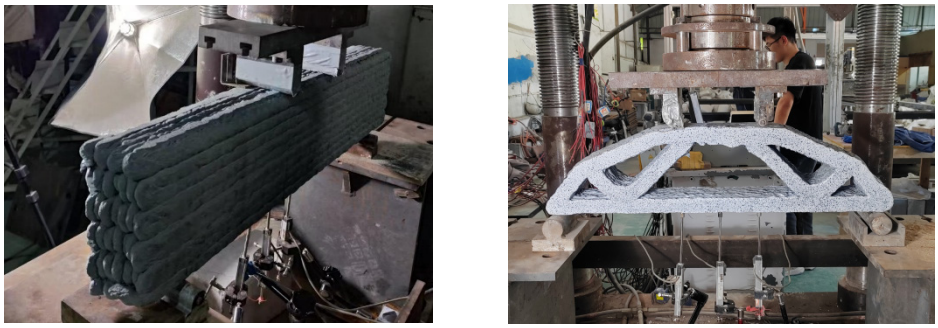
The beam geometry, reinforcement layout, and loading arrangement are shown in Figure 5. Four-point-bending tests were conducted using a 300 t servo-hydraulic testing machine under displacement control at 1 mm/min. The support span was 800 mm, and the two loading points were separated by 200 mm, resulting in two 300 mm shear spans and a 200 mm constant-moment region. A preload of approximately 0.2–0.3 kN was applied before formal loading to eliminate clearances in the loading system. Linear variable differential transformers (LVDTs) recorded vertical displacements beneath the two loading points and at midspan. Digital image correlation (DIC) was applied to one beam face to monitor the longitudinal strain field and crack localization, with images acquired at approximately 10 s intervals. Representative test arrangements for the reference and optimized beams are

shown in Figure 6. One structural beam was tested for each configuration (Ref, TO1, TO2, TO1-R and TO2-R). The percentage comparisons therefore describe the responses of the tested specimens rather than statistically estimated mean effects.



(**a**) (**b**)

Figure 5. Reinforcement layout and loading configuration: (**a**) TO1-R; (**b**) TO2-R.



(**a**) (**b**)

Figure 6. Four-point bending test setup: (**a**) full-section reference beam; (**b**) topology-optimized beam.

Small fabrication deviations in the external beam width and depth were corrected before comparison. For each specimen, the measured external dimensions b_{m} and h_{m} were used to calculate the envelope section modulus $Z_{\mathrm{m}} = b_{\mathrm{m}}h_{\mathrm{m}}^2/6$, while the nominal value was $Z_0 = b_0h_0^2/6$, where b_0 = 100 mm and h_0 = 200 mm. The corrected load was calculated as $P = P_{\mathrm{raw}}(Z_0/Z_m)$. This correction accounts only for deviations of the external beam envelope caused by fabrication and does not compensate for material removed by topology optimization. The actual ($b_{\mathrm{m}} \times h_{\mathrm{m}}$) dimensions were 102 × 202, 101 × 201, 97 × 203, 103 × 200, and 99 × 205 mm^2 for Ref, TO1, TO2, TO1-R, and TO2-R, respectively. The resulting Z0/Zm factors were 0.9611, 0.9803, 1.0007, 0.9709, and 0.9614. This approximate external-envelope correction changed each individual load by at most 3.9%.

2.5. Evaluation Metrics

The flexural response was characterized by the peak load P_{u}, the corresponding midspan deflection δ_{p}, and the post-peak deflection $\delta_{0.6}$, defined as the first deflection at which the descending load reached $0.6P_{\mathrm{u}}$. The energy absorption up to this state was calculated from the area under the corrected load–deflection curve, $W_{0.6} = \int_0^{\delta_{0.6}} P(\delta)d\delta$.

Because the optimized beams contained different amounts of ECC after printing, material utilization was additionally evaluated using the measured as-built retained-area ratio R_{a}. Peak-load and energy efficiencies relative to the full-section reference were expressed as $\eta_P = (P_u/R_a)/P_{u,\mathrm{Ref}}$ and $\eta_W = (W_{0.6}/R_a)/W_{0.6,\mathrm{Ref}}$, respectively, where $R_{\mathrm{a,Ref}}$ = 1. These normalized quantities are used only to evaluate material efficiency and do not replace the absolute structural response. These indices describe load or absorbed

energy per relative retained planar area; they do not assume a linear capacity–area law or establish mass-specific structural efficiency.

3. Experimental Results and Discussion

3.1. Load-Deflection Response and Crack Evolution

Figure 7 compares the load–deflection responses with the corresponding DIC longitudinal-strain fields at three representative loading stages. State A represents a stable pre-peak stage after the development of visible cracking, state B corresponds to the peak load, and state C represents the post-peak stage close to $0.6P_u$. The circles indicate the critical regions where crack localization or interface separation developed and subsequently contributed to final failure. The circled regions in Figure 7b(B),c(C),d(B) also show visible surface separation along printable connections. The DIC fields show the distribution of longitudinal surface strain (ε_{xx}), with a consistent color scale ranging from −0.02 to 0.08 applied to all specimens. Regions of high positive strain indicate tensile strain localization associated with crack development.

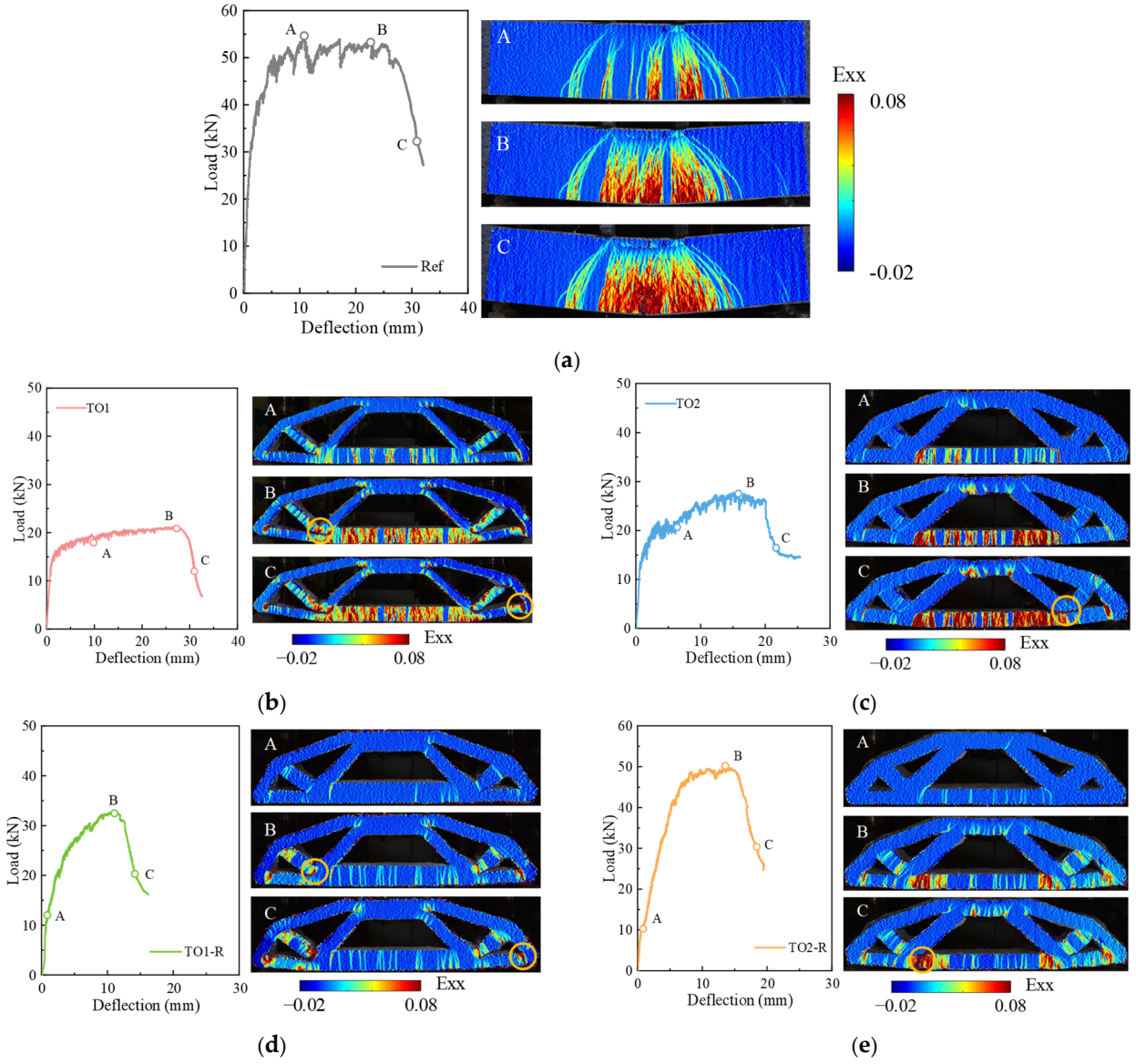


Figure 7. Load-deflection responses and DIC crack patterns of beams: (**a**) Ref; (**b**) TO1; (**c**) TO2; (**d**) TO1-R; (**e**) TO2-R.

The full-section Ref specimen exhibited distributed flexural cracking over the constant-moment region and adjacent beam segments. This response reflects the multiple-cracking capacity of the printed ECC and provides the baseline against which the more discrete force-transfer behavior of the optimized beams can be evaluated.

TO1 developed extensive tensile strain along the continuous lower chord. Multiple localized strain bands formed progressively over a relatively long region, allowing deformation to continue accumulating while the load remained stable. At later loading stages, localization became more pronounced around the intersections between the inclined members and the lower chord and near the support-side end connection. After steel-wire mesh was introduced, the crack pattern of TO1-R became substantially more localized. Distributed tensile deformation of the lower chord was restrained, whereas higher strain concentrations developed around the lower-chord connections. Compared with TO1, TO1-R showed a clear shift from distributed lower-chord deformation to more localized deformation near the member connections.

TO2 exhibited a more concentrated crack pattern than TO1 even before reinforcement. Compared with TO1, the high-strain region was distributed over a shorter portion of the lower chord. TO2-R retained a relatively stable deformation process after reinforcement. Although strain localization increased near the intersections of the inclined members and lower chord, the strain field remained less localized than that of TO1-R near the peak state. Overall, the DIC results show that reinforcement changed not only the magnitude of deformation but also its spatial distribution within the optimized beams. Because the steel-wire bundles were embedded within the ECC, internal wire rupture and steel–ECC debonding could not be conclusively distinguished from the available experimental observations.

3.2. Bearing Capacity, Deformation and Energy Absorption

Table 3 shows that steel-wire mesh substantially increased the flexural resistance of both optimized configurations, but its influence on deformation and energy absorption depended strongly on the printable topology. For TO1, reinforcement increased the peak load by 53.7%, but the peak and post-peak deflections decreased by 56.9% and 53.3%, respectively. Consequently, $W_{0.6}$ decreased by 36.8%. The reinforcement therefore produced a clear trade-off between resistance and deformation capacity in this configuration. Together with the DIC results in Figure 7, these data show that reinforcement changed TO1 from a high-deformation response with distributed cracking to a stronger but more localized response. The reduction in $W_{0.6}$ therefore reflects earlier structural localization rather than a change in the intrinsic tensile ductility of the ECC.

Table 3. Experimental flexural response parameters.

Specimen	P_u (kN)	δ_p (mm)	$\delta_{0.6}$ (mm)	$W_{0.6}$ (J)
Ref	54.94	10.74	30.76	1465.5
TO1	21.21	26.51	30.81	584.5
TO2	27.71	14.99	21.55	491.1
TO1-R	32.61	11.42	14.39	369.3
TO2-R	50.22	13.50	18.43	723.0

For TO2, reinforcement increased the peak resistance by 81.2%, while the peak deflection decreased by only 9.9%. More importantly, $W_{0.6}$ increased by 47.2%, in contrast to the decrease observed for TO1. Thus, TO2-R achieved a large increase in resistance while retaining most of the peak deformation capacity of TO2. The different responses of TO1-R and TO2-R show that reinforcement effectiveness cannot be determined from reinforcement

ratio alone. Both specimens contained the same steel area and nominal reinforcement ratio, yet they exhibited markedly different changes in peak resistance, deformation, and energy absorption. The effect of reinforcement is therefore strongly dependent on the printable topology. The underlying cause of this difference is further examined using the numerical damage patterns in Section 4.2.

Compared with the full-section reference, TO2-R reached 91.4% of the reference peak load despite containing substantially less printed ECC. TO1-R reached a smaller fraction of the reference capacity, although its strength was still considerably higher than that of its unreinforced counterpart. Absolute structural performance alone, however, does not fully represent the efficiency of the optimized configurations because the amount of material retained after printing differed among specimens.

3.3. Material Retention and Structural Efficiency

The material quantity of the printed beams differed from that of the reconstructed digital geometries. Figure 8 compares R_d and R_a. TO1 and TO1-R had the same designed ratio of 30.7%, whereas their as-built ratios were 31.6% and 33.2%, respectively. The corresponding values for TO2 and TO2-R increased from the common designed ratio of 34.7% to 36.2% and 42.0%. These deviations may result from filament spreading, local width variations, overlaps and deposition irregularities. The increase in Ra does not, by itself, identify where the additional ECC is located or whether it improves a critical connection.

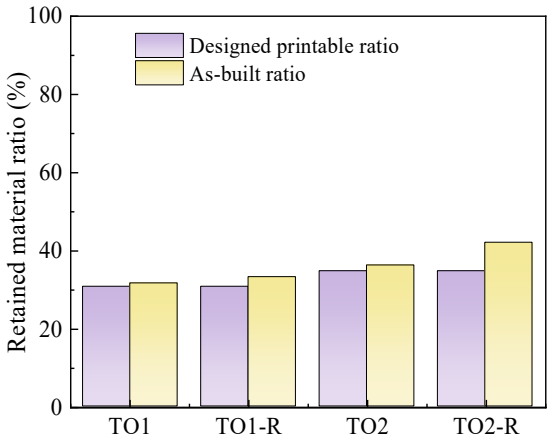


Figure 8. Designed and as-built retained-area ratios.

For TO2-R, the increase in as-built retained area from 36.2% to 42.0% must be considered when evaluating the effect of reinforcement. Its 81.2% absolute increase in peak load relative to TO2 includes both the contribution of the steel-wire mesh and the additional ECC deposited during fabrication. Figure 9 therefore presents load–deflection curves normalized by Ra as a supplementary material-utilization comparison. After this normalization, reinforcement increased the peak response of TO1 by 46.3% and that of TO2 by 56.2%. The area-normalized comparison indicates higher peak resistance per relative retained ECC area after reinforcement. TO2-R reached an area-normalized peak resistance of 119.57 kN, compared with 54.94 kN for Ref, giving a descriptive peak-load efficiency index of approximately 2.18 relative to Ref. This ratio is based on retained planar area, not measured mass, and cannot isolate the effects of local material redistribution.

Peak resistance alone, however, does not capture deformation efficiency. Figure 10 compares η_P and η_W. Unreinforced TO1 lies above the $\eta_W = 1$ reference line because its distributed lower-chord cracking provided high energy absorption relative to its small material quantity. Reinforcement shifted TO1-R strongly toward higher η_P, but η_W decreased from 1.262 to 0.759 as deformation localized earlier. TO2 followed the opposite tendency.

Reinforcement increased η_P from 1.393 to 2.176 while also increasing η_W from 0.926 to 1.175. TO2-R therefore lies in the region where both peak-load and energy efficiencies exceed those of Ref. The relative performance of TO1 and TO2 changed after reinforcement was introduced, showing that printable topology and reinforcement cannot be evaluated independently. Both should be considered when load capacity and deformation are design objectives.

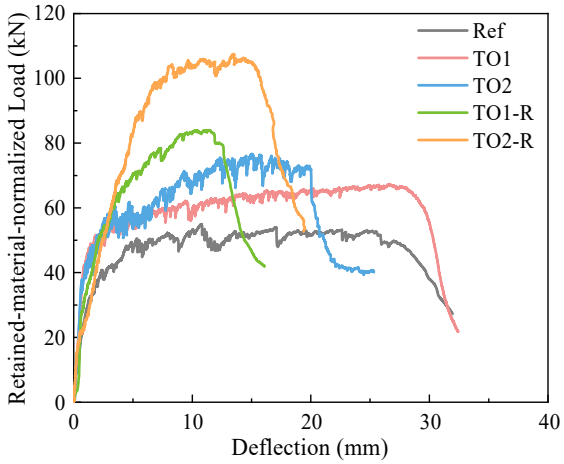


Figure 9. Retained-area-normalized load–deflection responses.

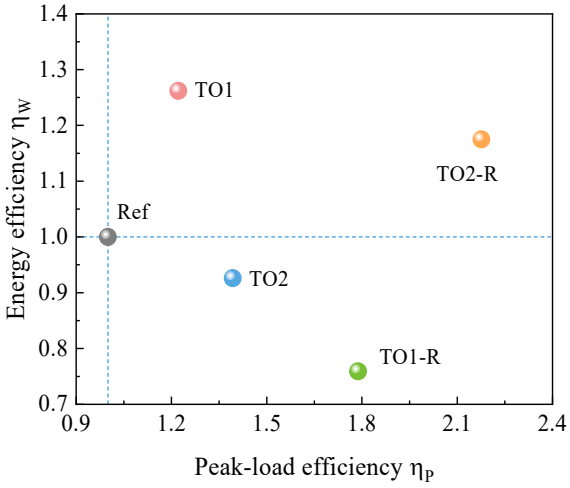


Figure 10. Peak-load and energy efficiency indices.

4. Numerical Simulation

4.1. Model Construction

4.1.1. Material Constitutive Models

The nonlinear response of 3DP-ECC was represented using the concrete damaged plasticity (CDP) model. The tensile constitutive relationship reproduced the experimentally measured response, consisting of an initial elastic stage followed by strain hardening and subsequent tensile softening. The compressive relationship included the nonlinear ascending and post-peak descending branches shown in Figure 11. The remaining CDP flow-potential and yield-surface parameters followed commonly adopted values in previous numerical studies of 3DP-ECC [37]. The ECC elastic modulus was set to 20 GPa and Poisson's ratio to 0.20. The CDP parameters were $\psi = 30°$, flow eccentricity = 0.1, $f_{b0}/f_{c0} = 1.16$, $K_c = 0.667$, and viscosity = 0.0005 [38]. For the steel-wire mesh, an elastic-

brittle tensile model was adopted using an elastic modulus of 150 GPa and an ultimate tensile strain of 2.0%, as illustrated in Figure 11c.

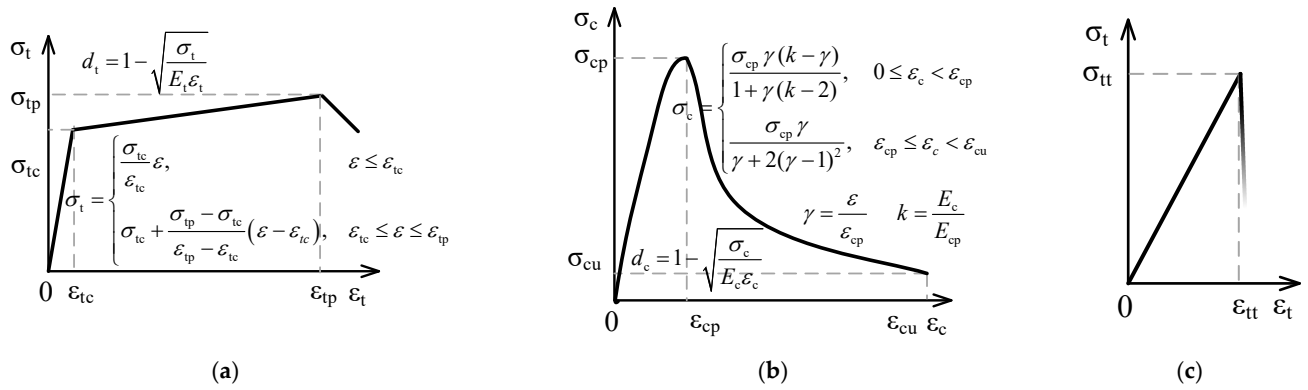


Figure 11. Constitutive representations used in the FE model: (**a**) tensile response of 3DP-ECC; (**b**) compressive response of 3DP-ECC; and (**c**) tensile response of steel-wire mesh.

4.1.2. Printed Interfaces

The finite-element geometry was reconstructed according to the actual toolpath layouts of TO1 and TO2 rather than generated as a continuous monolithic frame. Therefore, the start/stop discontinuities, member junctions, and interfaces produced during printable-path reconstruction were retained in their designed positions. This treatment allowed local separation to develop at locations that would otherwise be artificially constrained if the entire optimized beam were modeled as a single continuous ECC part.

Two types of printed interfaces were considered. Interfaces between adjacent filament regions and at the reconstructed path junctions were represented by zero-thickness eight-node cohesive elements (COH3D8), as indicated in Figure 12a,b [39]. Interfaces between adjacent deposited layers were modeled using cohesive surface interaction. Normal hard contact was additionally assigned to prevent penetration after interface opening, while a friction coefficient of 0.5 was used to represent residual shear transfer following partial or complete cohesive degradation [40].

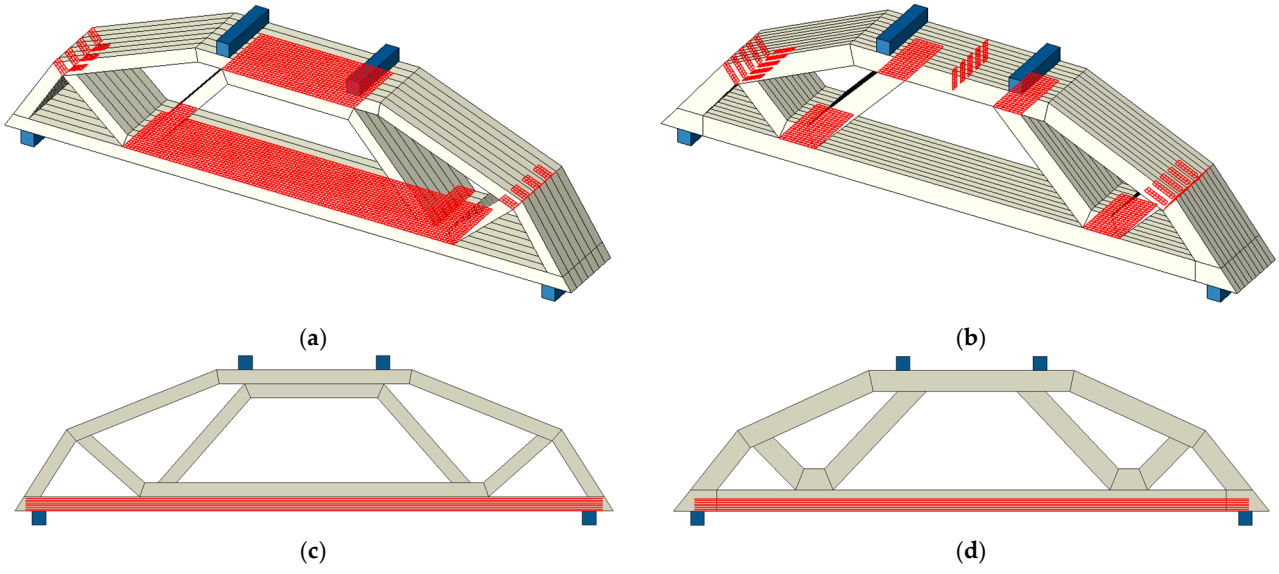


Figure 12. Numerical representation of printed interfaces and reinforcement: (**a**) TO1 interfaces; (**b**) TO2 interfaces; (**c**) TO1-R reinforcement; (**d**) TO2-R reinforcement.

A linear traction–separation relationship, $\mathbf{t} = \mathbf{K}\boldsymbol{\delta}$, was adopted before damage initiation. The penalty stiffness in the normal and two shear directions was 5×10^{10} N/m^3 [38]. Damage initiation was governed by the maximum nominal stress criterion,

$$\max\left\{\frac{\langle t_n \rangle}{t_n^0}, \frac{|t_s|}{t_s^0}, \frac{|t_t|}{t_t^0}\right\} = 1 \quad (1)$$

where t_n^0, t_s^0, t_t^0 are the nominal interface strengths. Direct tensile and shear tests were conducted on the printed ECC interlayer interfaces following the methods in the literature [41,42], with three specimens for each test method. The measured mean normal and shear bond strengths were 2.47 and 5.04 MPa, respectively. Accordingly, normal and shear cohesive strengths of 2.5 and 5.0 MPa were adopted in the baseline FE model [43]. After initiation, the cohesive stiffness was progressively degraded until the prescribed failure separation of 1.6 mm was reached [38], as illustrated in Figure 13. The same cohesive parameters were assigned to the inter-filament elements and layerwise cohesive interactions. The scalar stiffness-degradation variable (SDEG) was used to identify interface degradation, where SDEG = 0 represents an intact interface and SDEG = 1 represents complete loss of cohesive stiffness.

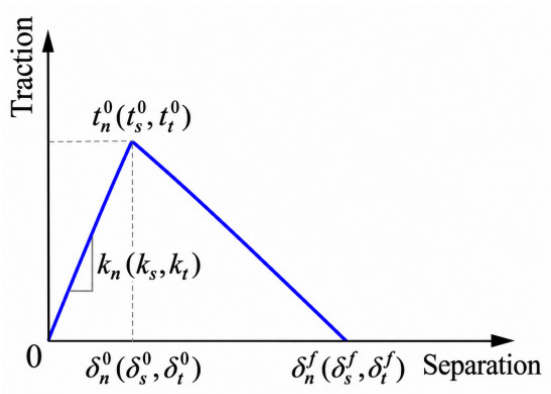


Figure 13. Cohesive traction-separation law.

4.1.3. Geometry and Boundary Conditions

ABAQUS was selected because it enables the nonlinear behavior of ECC, cohesive degradation of printed interfaces, and embedded steel reinforcement to be represented within a unified FE framework. The numerical analyses were performed using the Static, General procedure. The 3DP-ECC matrix was discretized using eight-node reduced-integration solid elements (C3D8R). A mesh convergence analysis was conducted to evaluate the influence of element size on the numerical results. Considering the balance between numerical accuracy and computational cost, a characteristic element size of 5 mm was adopted for all FE models. The steel-wire mesh was represented by its 40 longitudinal wire bundles using two-node truss elements (T3D2). The wire bundles were embedded within the surrounding ECC. Figure 12c,d shows the reinforcement layouts adopted for TO1-R and TO2-R. In both configurations, the 40 steel-wire bundles were distributed within the bottom 20 mm region, giving an equivalent reinforcement centroid approximately 10 mm above the beam bottom. The FE geometry followed the designed printing dimensions. The loading and support regions reproduced the experimental four-point-bending configuration.

4.2. Model Validation

Figure 14 compares the experimental and numerical load-deflection responses and the corresponding numerical tensile-damage and interface-degradation patterns. The simulations reproduced the relative response of the four optimized configurations, including

the increase in resistance after reinforcement and the different deformation characteristics of TO1 and TO2. In these plots, DamageT denotes the ABAQUS tensile-damage output variable, while SDEG indicates cohesive stiffness degradation as defined in Section 4.1.2.

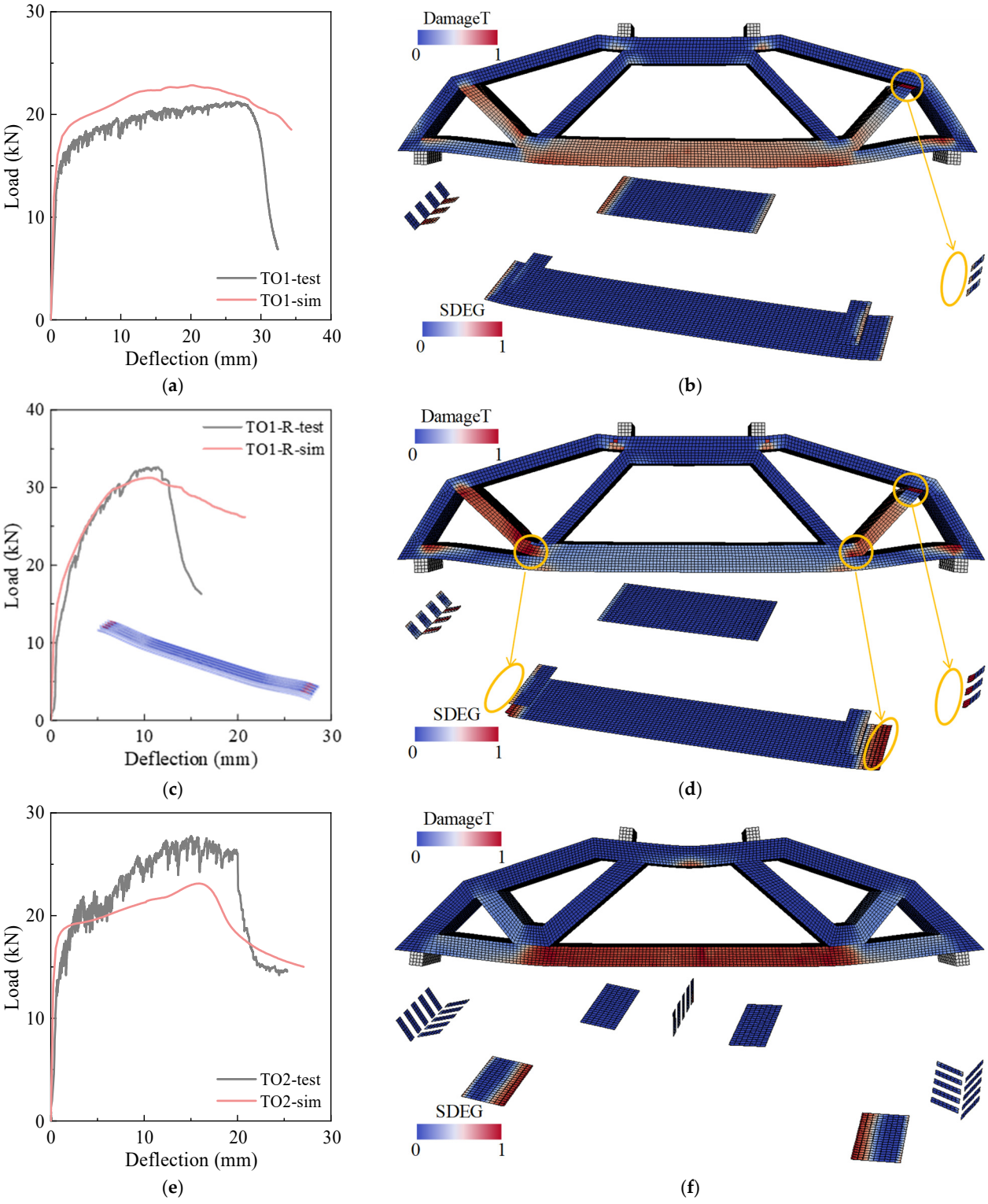
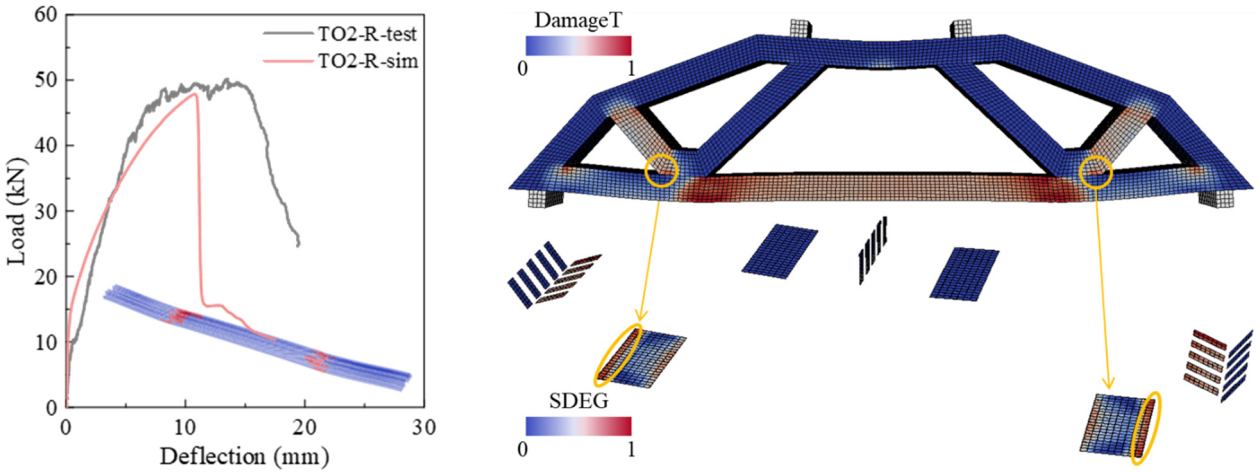


Figure 14. *Cont.*



(**g**) (**h**)

Figure 14. Experimental and numerical responses with simulated damage patterns: (**a**,**b**) TO1; (**c**,**d**) TO1-R; (**e**,**f**) TO2; (**g**,**h**) TO2-R.

A direct comparison based solely on absolute peak load is affected by the unavoidable geometric differences between the numerical and experimental specimens. The numerical models represent the designed printable geometry, whereas filament spreading, trajectory overlap, corner accumulation, and local deformation during fabrication altered both the amount and spatial distribution of ECC in the physical specimens. For each printable configuration, the reinforced and unreinforced FE models shared the same ECC geometry, allowing the reinforcement effect to be evaluated without the influence of fabrication-induced differences in material distribution. In addition, the modeled width of TO1 was 105 mm, compared with the nominal 100 mm reference width. The numerical retained-volume ratio used for comparison accounts for this modeled ECC geometry. Quantitative validation was therefore additionally performed using the retained-material-normalized peak resistance. For the experiments, the normalized resistance was defined as $\overline{P}_{u,\mathrm{test}} = P_{u,\mathrm{test}}/R_a$, where the experimental loads had already been corrected to the nominal external envelope using the section-modulus correction described in Section 2.4. For the numerical models, $\overline{P}_{u,\mathrm{FE}} = P_{u,\mathrm{FE}}/R_{\mathrm{FE}}$, where R_{FE} is the volume of the numerical ECC geometry relative to the nominal 100 mm × 200 mm reference beam.

As summarized in Table 4, the absolute differences in normalized peak resistance ranged from 1.3% to 12.1%, with a mean absolute deviation of approximately 7.3%. Particularly close agreement was obtained for TO1 and TO1-R. The larger deviations for TO2 and TO2-R may be partly attributed to differences between the idealized FE geometries and the as-built geometries affected by filament spreading and deposition irregularities. Importantly, the reinforced and unreinforced FE models of each configuration employed identical ECC geometries and interface arrangements, with steel reinforcement as the only variable. The simulations showed that steel-wire mesh increased the peak resistance of TO1 and TO2 by 36.8% and 95.3%.

Table 4. Comparison of retained-material-normalized peak resistance.

Specimen	$\overline{P}_{u,\mathrm{test}}$ (kN)	$\overline{P}_{u,\mathrm{FE}}$ (kN)	Difference
TO1	67.12	70.87	5.6%
TO2	76.55	68.63	−10.3%
TO1-R	98.22	96.98	−1.3%
TO2-R	119.57	134.02	12.1%

Several additional sources contribute to the remaining differences. First, the numerical geometry retains ideal member boundaries and prescribed interface locations, whereas the printed specimens inevitably contained deviations in member width, corner radius, joint shape, and local alignment. These imperfections are particularly influential in topology-optimized beams because force transfer is concentrated into a relatively small number of narrow members and junctions. Second, identical cohesive properties were assigned to all interfaces, while actual bond quality varies spatially with extrusion pressure, local contact area, deposition history, and the presence of start/stop locations. Finally, the embedded treatment of the wire bundles assumes perfect steel-ECC compatibility before wire rupture and cannot reproduce local mesh slip, progressive engagement of individual wires, or sequential rupture within a bundle. Accordingly, the model is used to compare peak-load trends and critical damage locations, not to quantitatively reproduce post-peak energy absorption. The abrupt simulated drop of TO2-R and the mismatch in the descending response of TO1-R in Figure 14 illustrate this limitation.

The numerical damage patterns provide further validation of the model and clarify the change in failure mechanism after reinforcement. For TO1, tensile damage was distributed mainly along the lower chord, with only limited interface degradation near the support-side end region. After reinforcement, TO1-R developed pronounced damage at the diagonal-to-lower-chord connections and at the outer support-side connection, consistent with the stronger localization observed by DIC. A similar change occurred in TO2. The unreinforced TO2 model was governed mainly by tensile damage along the lower chord, whereas TO2-R developed pronounced interface degradation at the diagonal-to-lower-chord connections. These results indicate that the steel-wire mesh increased the tensile capacity of the lower chord, allowing a larger tensile force to be transferred through the adjoining inclined members. The increased force demand was concentrated at the diagonal-to-chord connections, where the load path changed direction and local tensile and shear stresses developed. Consequently, the critical region shifted from distributed cracking of the lower chord toward localized connection and interface damage. This mechanism explains the experimentally observed reduction in deformation capacity of TO1-R and the different reinforcement response of TO1 and TO2.

4.3. Parametric Analysis

The validated models were used to investigate two parameters governing tensile-force transfer in the optimized beams: nominal reinforcement ratio and printed-interface strength. The model notation used in this section identifies both parameters. For example, in the notation TO1-R0.05-B2.5, TO1 denotes the printable topology, R0.05 denotes a nominal reinforcement ratio of 0.05%, and B2.5 denotes a normal cohesive strength of 2.5 MPa. Reinforcement ratios of 0.05%, 0.10%, and 0.15% were examined while maintaining the baseline normal cohesive strength at 2.5 MPa. In the interface-strength study, the reinforcement ratio was fixed at 0.10%, while the normal bond strength was varied among 1.0, 2.5, and 4.0 MPa. All remaining model parameters were kept unchanged. The shear cohesive strengths were maintained at twice the corresponding normal strength throughout the analysis. This ratio is consistent with the experimentally measured ratio in this study and is supported by similar findings as well [44,45]. This analysis evaluates coupled changes in overall interface behavior. This is a targeted, one-factor-at-a-time exploratory analysis of the two modeled geometries, not a coupled multivariable optimization or a statistically generalizable design study.

4.3.1. Effect of Reinforcement Ratio

Figure 15 compares the influence of reinforcement ratio on the two printable configurations. TO1 exhibits only moderate sensitivity to additional reinforcement. Increasing ρ_s from 0.05% to 0.10% raises the peak load by 9.1%, while a further increase to 0.15% provides only another 4.8%. Thus, tripling the steel ratio produces an overall strength gain of only 14.3%, while the peak deflection continuously decreases. The similar damage patterns in Figure 15b explain this limited additional strength gain. At both 0.05% and 0.15%, interface opening first develops at the support-side tensile diagonal at location a. This separation interrupts the direct tensile-force-transfer path through the diagonal. Load is subsequently redistributed toward the outer support-side region, where the combined tensile and shear demand increases sharply and produces the secondary failure at b. Because the same interface-controlled sequence occurs at both reinforcement levels, increasing ρ_s does not remove the governing weak region. This explains why increasing ρ_s from 0.05% to 0.15% produces only a 14.3% increase in peak resistance.

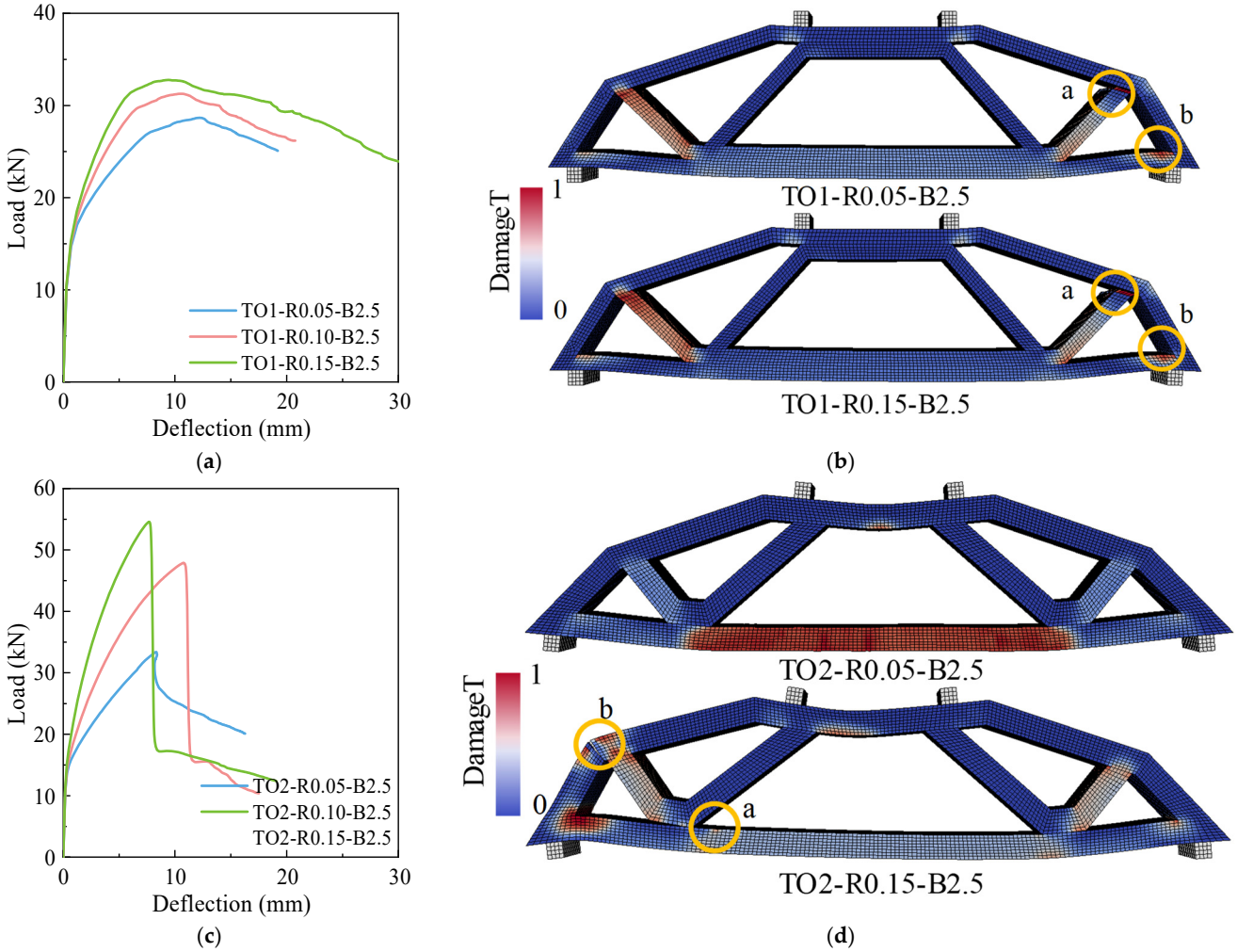


Figure 15. Effect of reinforcement ratio on load-deflection response and failure mode: (**a**,**b**) reinforced TO1 series beams; (**c**,**d**) reinforced TO2 series beams.

TO2 exhibits a substantially different reinforcement response. Increasing ρ_s from 0.05% to 0.10% raises the peak resistance by 43.5%, and the 0.15% model shows a 63.5% increase in resistance relative to the 0.05% model. The larger gain from 0.05% to 0.10% indicates that, at low reinforcement ratios, TO2 can transfer the additional tensile force more effectively than TO1. The governing failure mechanism, however, changes as the reinforcement ratio

increases. TO2-R0.05-B2.5 does not develop pronounced interface separation. Instead, tensile damage is distributed along a broad region of the lower chord, and the response ultimately becomes controlled by rupture of the steel-wire reinforcement. At this low steel ratio, the tensile capacity of the reinforced chord therefore remains the limiting component.

By contrast, TO2-R0.15-B2.5 is governed by interface damage rather than reinforcement rupture. The first critical event occurs at a, where the horizontal inter-filament interface between the compression diagonal and the lower chord undergoes shear-dominated sliding. Loss of restraint at this interface permits the diagonal to displace outward, thereby amplifying local deformation and mixed tensile–shear demand in the outer connection. This produces the subsequent failure at b. The response has therefore shifted from reinforcement-controlled failure at 0.05% to interface-controlled failure at the higher reinforcement ratio. This transition also explains the non-monotonic deformation response. The 0.10% model reaches its peak at a deflection of approximately 10.8 mm, about 40% greater than that of the 0.15% model, while retaining substantially more resistance than the 0.05% case. Increasing reinforcement beyond the level that can be supported by the surrounding printed interfaces therefore raises peak strength but accelerates interface localization and reduces deformation capacity.

The comparison of TO1 and TO2 demonstrates that reinforcement ratio cannot be selected independently of printable topology. TO1 remains controlled by essentially the same support-side tensile-transfer discontinuity over the investigated reinforcement range, whereas TO2 benefits strongly from added reinforcement until the governing weakness migrates to a horizontal interface near the diagonal-to-chord transition. For such members, continuity of the tensile load path, particularly the avoidance of printing start/stop discontinuities at critical tensile connections, should be considered together with the reinforcement amount when interface damage becomes governing.

4.3.2. Effect of Interface Strength

The interface-strength study was intended to represent variations in bond quality that can arise during printing. The 1.0 MPa case represents a poorly bonded interface that may result from insufficient filament contact, excessive toolpath spacing, or unfavorable deposition conditions. The 4.0 MPa case represents a hypothetical high-bond condition below the measured ultimate tensile strength of ECC.

TO1 is highly sensitive when the interface changes from weak to moderate bonding. Increasing the normal strength from 1.0 to 2.5 MPa raises the peak resistance by 52.1%, while the corresponding peak deformation increases to more than four times its value at 1.0 MPa. A further increase from 2.5 to 4.0 MPa produces only an 11.4% additional strength gain, indicating a pronounced reduction in marginal benefit. The failure sequence in Figure 16b explains this behavior. With a 1.0 MPa interface, separation initiates almost simultaneously at the two diagonal-to-lower-chord connections marked a. These joints are required to transfer forces from the inclined members into the longitudinal tensile chord; premature debonding therefore disconnects the principal load-transfer system before the reinforcement can be fully mobilized. Increasing the interface strength suppresses this early separation. At 4.0 MPa, the two internal chord connections remain intact, and failure is displaced toward the support-side portion of the topology: localization first develops at a around the outer inclined-member connection and subsequently reaches the end region b.

TO2 shows an even stronger weak-interface effect. Increasing the normal cohesive strength from 1.0 to 2.5 MPa approximately doubles the peak resistance, while peak deformation increases to roughly 4.6 times. By contrast, increasing the strength from 2.5 to 4.0 MPa changes the peak resistance by only about 3.5%, indicating that the global response has already become largely insensitive to further bond enhancement. At 1.0 MPa, interface

degradation in TO2 begins simultaneously at the two diagonal-to-lower-chord connections marked a in Figure 16d. Once these lower connections lose continuity, the remaining force is redistributed through the upper frame. Damage then propagates to the upper transition region b and subsequently to the support-side outer junction c, resulting in an early loss of structural resistance. The weak interfaces therefore fragment the optimized force-transfer network before either the reinforced lower chord or the ECC members reach their available capacity. In contrast, the 4.0 MPa TO2 model exhibits no comparable localized interface failure at these critical junctions. Damage is concentrated primarily within the lower tensile chord and adjacent ECC regions, indicating that the governing mechanism has changed from interface-controlled separation to member-controlled tensile damage. Once this transition has occurred, further interface strengthening cannot produce a comparable increase in global resistance.

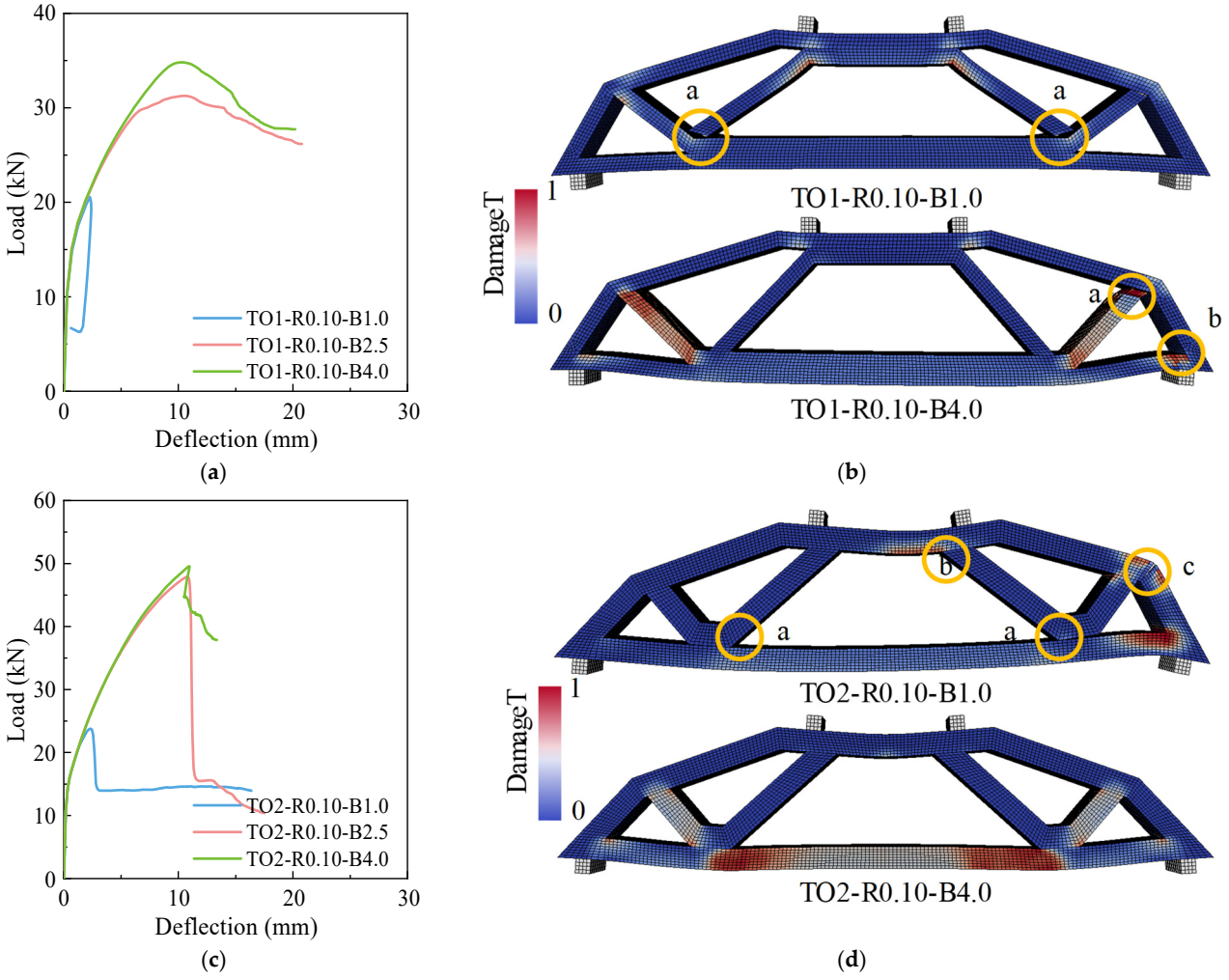


Figure 16. Effect of printed-interface strength on load–deflection response and failure mode: (**a**,**b**) reinforced TO1 series beams; (**c**,**d**) reinforced TO2 series beams.

The results indicate a clear change in response once sufficient interface strength is reached. Weak interfaces interrupt the intended load path before the ECC members and reinforcement can develop their available capacity. Increasing the normal strength from 1.0 to 2.5 MPa therefore produces a large improvement, whereas the benefit becomes much smaller above 2.5 MPa. In practical path planning, extrusion discontinuities and low-contact interfaces should be avoided, particularly at diagonal-to-chord transitions.

The low reinforcement ratio is advantageous for 3D printing, as it helps minimize disturbance to interlayer bonding and the formation of reinforcement-induced voids, while facilitating mesh integration during extrusion. For larger-scale applications, continuous mesh placement, reinforcement anchorage, and coordination between mesh installation and printing paths require further consideration. Although the present study investigated two printable configurations, the optimal coordination between topology, printing paths, and reinforcement layout remains to be established. Future research should therefore focus on their integrated design, particularly maintaining continuous tensile chords, avoiding extrusion start/stop locations at critical connections, and improving filament continuity within joint regions. The scalability of these strategies and the long-term durability of embedded steel reinforcement should also be evaluated.

The present experiments involved one beam per configuration, one ECC batch, laboratory-scale specimens, and one four-point-bending load case. Consequently, the observed reinforcement and energy-absorption trends are specific to these tested prototypes. The FE parametric results likewise depend on idealized geometry, uniform interface properties, and perfect steel–ECC bond; broader design guidance requires replicated testing and validation under other scales and loading conditions.

5. Conclusions

This study experimentally and numerically investigated steel-wire-mesh reinforcement of two printable topology-optimized 3DP-ECC beam configurations. The numerical model explicitly reproduced the printable geometry, extrusion discontinuities, and inter-filament and interlayer interfaces, and was subsequently used to investigate reinforcement ratio and interface strength. Because only one structural specimen was tested per configuration, the experimental results describe the measured prototype responses rather than population-average reinforcement effects. The main conclusions are as follows.

(1) Steel-wire mesh substantially improved the load-carrying capacity of both topology-optimized beams, but its effect on deformation depended strongly on the printable configuration. Reinforcement increased the experimental peak loads of TO1 and TO2 by 53.7% and 81.2%, respectively; after normalization by the measured as-built retained-area ratio, the corresponding peak-resistance gains were 46.3% and 56.2%. TO1 exhibited a 36.8% reduction in energy absorption after reinforcement, whereas TO2 exhibited a 47.2% increase. TO2-R consequently reached 91.4% of the full-section reference peak load with an as-built retained-material ratio of only 42.0%.

(2) Reinforcement changed the failure mode of the optimized beams. Unreinforced specimens were dominated by distributed lower-chord cracking, whereas reinforced specimens showed stronger localization at diagonal-to-chord connections and support-side interfaces. The FE results indicate that these regions became critical as the tensile force carried by the reinforced lower chord increased.

(3) The interface-explicit FE models captured the main peak-resistance trends and the simulated critical damage locations. The simulations predicted interface degradation near the same critical connection regions where strong strain localization was observed experimentally. The results indicate that connection force transfer and printed-interface capacity should be considered when selecting the reinforcement level of topology-optimized 3DP-ECC members. Once these regions become the governing weakness, additional longitudinal reinforcement offers limited benefit.

(4) Within the investigated model ranges, the effect of reinforcement ratio differed between the two printable configurations. Tripling the reinforcement ratio increased peak resistance by only 14.3% for TO1 but by 63.5% for TO2, with the heavily reinforced TO2 eventually becoming interface-controlled. Increasing normal interface

strength from 1.0 to 2.5 MPa markedly improved both configurations, whereas further strengthening to 4.0 MPa produced only limited gains. Reinforcement level and interface quality should therefore be matched to the force-transfer capacity of the topology, with particular attention to diagonal-to-chord transitions and support-side nodes.

Future work should incorporate local steel–ECC bond slip and experimentally measured spatial variability of printed interfaces and ultimately integrate topology generation, printable-path planning, interface control, and reinforcement design within a unified optimization framework.

Author Contributions: Conceptualization, L.L.; methodology, M.L.; software, Y.J.; validation, Z.Y.; investigation, F.Y.; resources, A.M.; data curation, X.L.; writing—original draft preparation, M.L.; writing—review and editing, A.M., X.L.; visualization, F.T.; supervision, L.L. All authors have read and agreed to the published version of the manuscript.

Funding: This research was funded by the Fundamental Research Funds for the Central Universities.

Data Availability Statement: The data presented in this study are available from the corresponding author upon reasonable request.

Conflicts of Interest: Authors Zheng Yang and Xiang Li were employed by State Grid Electric Power Engineering Research Institute Co., Ltd. Author Fei Teng was affiliated with Shanghai Investigation, Design & Research Institute Co., Ltd. The authors declare no other conflicts of interest related to this study.

References

1. Baral, S.; Lande, I.; Vysochinskiy, D. Opportunities and Challenges Related to 3D Printed Concrete: A Review. *Buildings* **2026**, *16*, 2300. [CrossRef]
2. Du, G.; Qian, Y. Bio-inspired innovations in 3D concrete printing: Structures, materials and applications. *Appl. Mater. Today* **2024**, *41*, 102459. [CrossRef]
3. Girskas, G.; Kligys, M. 3D Concrete Printing Review: Equipment, Materials, Mix Design, and Properties. *Buildings* **2025**, *15*, 2049. [CrossRef]
4. Rehman, A.U.; Kim, J.-H. 3D Concrete Printing: A Systematic Review of Rheology, Mix Designs, Mechanical, Microstructural, and Durability Characteristics. *Materials* **2021**, *14*, 3800. [CrossRef]
5. Yago, D.; Cante, J.; Lloberas-Valls, O.; Oliver, J. Topology Optimization Methods for 3D Structural Problems: A Comparative Study. *Arch. Comput. Methods Eng.* **2021**, *29*, 1525–1567. [CrossRef]
6. Wu, J.; Sigmund, O.; Groen, J.P. Topology optimization of multi-scale structures: A review. *Struct. Multidiscip. Optim.* **2021**, *63*, 1455–1480. [CrossRef]
7. Haveroth, G.A.; Thore, C.J.; Correa, M.R.; Ausas, R.F.; Jakobsson, S.; Cuminato, J.A.; Klarbring, A. Topology optimization including a model of the layer-by-layer additive manufacturing process. *Comput. Methods Appl. Mech. Eng.* **2022**, *398*, 115203. [CrossRef]
8. Vantyghem, G.; De Corte, W.; Shakour, E.; Amir, O. 3D printing of a post-tensioned concrete girder designed by topology optimization. *Autom. Constr.* **2020**, *112*, 103084. [CrossRef]
9. Li, Y.; Wu, H.; Xie, X.; Zhang, L.; Yuan, P.F.; Xie, Y.M. FloatArch: A cable-supported, unreinforced, and re-assemblable 3D-printed concrete structure designed using multi-material topology optimization. *Addit. Manuf.* **2024**, *81*, 104012. [CrossRef]
10. Bi, M.; Tran, P.; Xia, L.; Ma, G.; Xie, Y.M. Topology optimization for 3D concrete printing with various manufacturing constraints. *Addit. Manuf.* **2022**, *57*, 102982. [CrossRef]
11. Yang, W.; Wang, L.; Ma, G.; Feng, P. An integrated method of topological optimization and path design for 3D concrete printing. *Eng. Struct.* **2023**, *291*, 116435. [CrossRef]
12. Hernández Vargas, J.; Sjölander, A.; Westerlind, H.; Silfwerbrand, J. Internal topology optimisation of 3D printed concrete structures: A method for enhanced performance and material efficiency. *Virtual Phys. Prototyp.* **2024**, *19*, 2346290. [CrossRef]
13. Silva, G.; Quispe, A.; Baldoceda, J.; Kim, S.; Ruiz, G.; Pando, M.A.; Nakamatsu, J.; Aguilar, R. Additive construction of concrete deep beams using low-cost characterization methods and FEM-based topological optimization. *Constr. Build. Mater.* **2024**, *418*, 135418. [CrossRef]
14. Salaimanimagudam, M.P.; Jayaprakash, J. Synergistic potential of topology optimization and lattice structures in concrete 3D printed beams. *Structures* **2025**, *76*, 108892. [CrossRef]

15. Yang, W.; Wang, L.; Hu, Y.; Sanjayan, J.; Ma, G. An integrated topology optimization method including manufacturing constraints for 3D printed fiber-reinforced concrete structures. *Mater. Lett.* **2024**, *355*, 135442. [CrossRef]
16. Mechtcherine, V.; Buswell, R.; Kloft, H.; Bos, F.P.; Hack, N.; Wolfs, R.; Sanjayan, J.; Nematollahi, B.; Ivaniuk, E.; Neef, T. Integrating reinforcement in digital fabrication with concrete: A review and classification framework. *Cem. Concr. Compos.* **2021**, *119*, 103964. [CrossRef]
17. Wu, Z.; Memari, A.; Duarte, J. State of the Art Review of Reinforcement Strategies and Technologies for 3D Printing of Concrete. *Energies* **2022**, *15*, 360. [CrossRef]
18. Kloft, H.; Sawicki, B.; Bos, F.; Dörrie, R.; Freund, N.; Gantner, S.; Gebhard, L.; Hack, N.; Ivaniuk, E.; Kruger, J.; et al. Interaction of reinforcement, process, and form in Digital Fabrication with Concrete. *Cem. Concr. Res.* **2024**, *186*, 107640. [CrossRef]
19. Liu, L.; Xiao, J.; Wu, Z. The effect of fiber content on the static and dynamic performance of PE-ECC. *Case Stud. Constr. Mater.* **2024**, *20*, e03041. [CrossRef]
20. Li, L.; Cai, Z.; Yu, K.; Zhang, Y.X.; Ding, Y. Performance-based design of all-grade strain hardening cementitious composites with compressive strengths from 40 MPa to 120 MPa. *Cem. Concr. Compos.* **2019**, *97*, 202–217. [CrossRef]
21. Wang, Y.; Hou, M.; Yu, J.; Xu, S.; Yu, K.; Zhang, Z. Experimental study on mechanical properties of ultra-high ductile cementitious composites. *Mater. Rep.* **2018**, *32*, 3535–3540. [CrossRef]
22. Yu, K.; Tang, Z.; Kuang, H.; Xue, Z.; Deng, B.; Ma, C.; Yu, J.; Wang, F. Exceptional high-temperature-resistant engineered geopolymer composites: Roles of LCP fiber and micromechanism. *Cem. Concr. Compos.* **2026**, *171*, 106639. [CrossRef]
23. Tang, Z.; Yu, K.; Li, X.; Jiang, F.; Ye, J.; Xue, Z.; Wang, T.; Dong, F. Towards rebar-free 3D printed high-strength engineered cementitious composites construction: Rheology characterization, material and structural element performances. *J. Build. Eng.* **2026**, *132*, 116721. [CrossRef]
24. Zhou, W.; McGee, W.; Gökçe, H.S.; Li, V.C. A bio-inspired solution to alleviate anisotropy of 3D printed engineered cementitious composites (3DP-ECC): Knitting/tilting filaments. *Autom. Constr.* **2023**, *155*, 105051. [CrossRef]
25. Chen, W.; Yu, J.; Ye, J.; Yu, J.; Li, V.C.; Yu, K. 3D printed high-performance fiber-reinforced cementitious composites (3DP-HPFRCC): Fresh, mechanical, and microstructural properties. *Autom. Constr.* **2026**, *181*, 106629. [CrossRef]
26. Mardani, A.; Hematibahar, M.; Özteber, S.; Qais, Q.A.A.; Khalil, I.; Gebre, T.H.; Elsheikh, A. Anisotropic Behavior of 3D-Printed Concrete: Interlayer Bonding, Pore Architecture, Reinforcement Limitations, and Durability Mechanisms. *Materials* **2026**, *19*, 3698. [CrossRef]
27. Chen, W.; Liu, Y.; Liang, L.; Xue, Z.; Basang, Z.; Shi, C.; Yu, J.; Yu, K. Machine learning-powered inverse design for 3D-printable engineered cementitious composites (3DP-ECC): Advancing insights into rheological properties. *Cem. Concr. Res.* **2026**, *209*, 108344. [CrossRef]
28. Chen, W.; Liang, L.; Li, X.; Yang, Z.; Shi, C.; Jiang, F.; Liao, G.; Liu, L.; Yu, J.; Yu, K. Sulfate resistance of 3D printed engineered cementitious composites (3DP-ECC): Deterioration mechanism and prediction models. *Cem. Concr. Compos.* **2026**, *172*, 106657. [CrossRef]
29. Tang, Z.; Yu, K.; Liu, L.; Xiao, J.; Jiang, Y.; Xue, Z. Prestressed high-strength ECC beams to achieve high flexural performance: Experiments and theoretical analysis. *Constr. Build. Mater.* **2026**, *537*, 147025. [CrossRef]
30. Gebhard, L.; Mata-Falcón, J.; Anton, A.; Dillenburger, B.; Kaufmann, W. Structural behaviour of 3D printed concrete beams with various reinforcement strategies. *Eng. Struct.* **2021**, *240*, 112380. [CrossRef]
31. Liu, M.; Zhang, Q.; Tan, Z.; Wang, L.; Li, Z.; Ma, G. Investigation of steel wire mesh reinforcement method for 3D concrete printing. *Arch. Civ. Mech. Eng.* **2021**, *21*, 24. [CrossRef]
32. Lin, M.; Ding, Y.; Yu, F.; Li, L.; Yu, K. Synergistic strengthening of 3D-printed ECC beams through steel-wire mesh and interfaces treatments. *Eng. Struct.* **2025**, *343*, 121205. [CrossRef]
33. Lin, M.; Li, L.; Jiang, F.; Ding, Y.; Yu, F.; Dong, F.; Yu, K. Automated reinforcement of 3D-printed engineered cementitious composite beams. *Autom. Constr.* **2024**, *168*, 105851. [CrossRef]
34. Wang, Q.; Yang, W.; Wang, L.; Bai, G.; Ma, G. Reinforcement design and structural performance for the topology optimized 3D printed concrete truss beams. *Eng. Struct.* **2025**, *332*, 120064. [CrossRef]
35. Wang, L.; Fan, H.; Wang, Q.; Bai, G.; Qu, Y.; Ma, G. Design method and force transmission mechanism of 3D printed concrete truss beams reinforced with 3D conical reinforcement. *Eng. Struct.* **2025**, *344*, 121368. [CrossRef]
36. Ye, J.; Cui, C.; Yu, J.; Yu, K.; Xiao, J. Fresh and anisotropic-mechanical properties of 3D printable ultra-high ductile concrete with crumb rubber. *Compos. Part B Eng.* **2021**, *211*, 108639. [CrossRef]
37. Du, G.; Qian, Y. Effects of printing patterns and loading directions on fracture behavior of 3D printed Strain-Hardening Cementitious Composites. *Eng. Fract. Mech.* **2024**, *304*, 110155. [CrossRef]
38. Ye, J.; Zhang, J.; Yu, J.; Yu, J.; Yu, K. Flexural behaviors of 3D printed lightweight engineered cementitious composites (ECC) slab with hollow sections. *Eng. Struct.* **2024**, *299*, 117113. [CrossRef]
39. An, N.; Wang, H.; Wang, P.; Xu, C.; Liu, M. Tension-compression anisotropic cohesion model for the interlayer interface of 3D-printed concrete compression specimens. *J. Build. Eng.* **2025**, *107*, 112800. [CrossRef]

40. Liu, H.; Xiao, J.; Ding, T. Flexural performance of 3D-printed composite beams with ECC and recycled fine aggregate concrete: Experimental and numerical analysis. *Eng. Struct.* **2023**, *283*, 115865. [CrossRef]
41. Yan, K.-T.; Wang, X.-P.; Ding, Y.; Li, L.-Z.; Bazarov, D.; Deng, B.-Y.; Nikolayevich, K.-S.; Yu, K.-Q. 3D-printed LC3-based lightweight engineered cementitious composites: Fresh state, harden material properties and beam performance. *J. Build. Eng.* **2024**, *93*, 109838. [CrossRef]
42. Wang, Z.; Chen, Z.; Xiao, J.; Ding, T. Experimental Study on Interfacial Shear Behavior of 3D Printed Recycled Mortar. *3D Print. Addit. Manuf.* **2024**, *11*, 1162–1174. [CrossRef]
43. Babafemi, A.J.; Kolawole, J.T.; Miah, M.J.; Paul, S.C.; Panda, B. A Concise Review on Interlayer Bond Strength in 3D Concrete Printing. *Sustainability* **2021**, *13*, 7137. [CrossRef]
44. Licciardello, L.; Reggia, A.; Metelli, G.; Plizzari, G.A. Experimental and numerical study on the inter-layer shear behavior of 3D printed concrete. *Mater. Struct.* **2026**, *59*, 274. [CrossRef]
45. Wang, H.; Shao, J.; Zhang, J.; Zou, D.; Sun, X. Bond shear performances and constitutive model of interfaces between vertical and horizontal filaments of 3D printed concrete. *Constr. Build. Mater.* **2022**, *316*, 125819. [CrossRef]

Disclaimer/Publisher's Note: The statements, opinions and data contained in all publications are solely those of the individual author(s) and contributor(s) and not of MDPI and/or the editor(s). MDPI and/or the editor(s) disclaim responsibility for any injury to people or property resulting from any ideas, methods, instructions or products referred to in the content.